Volume 5, Number 1 *October 2023*

Nanomaterials Science & Engineering

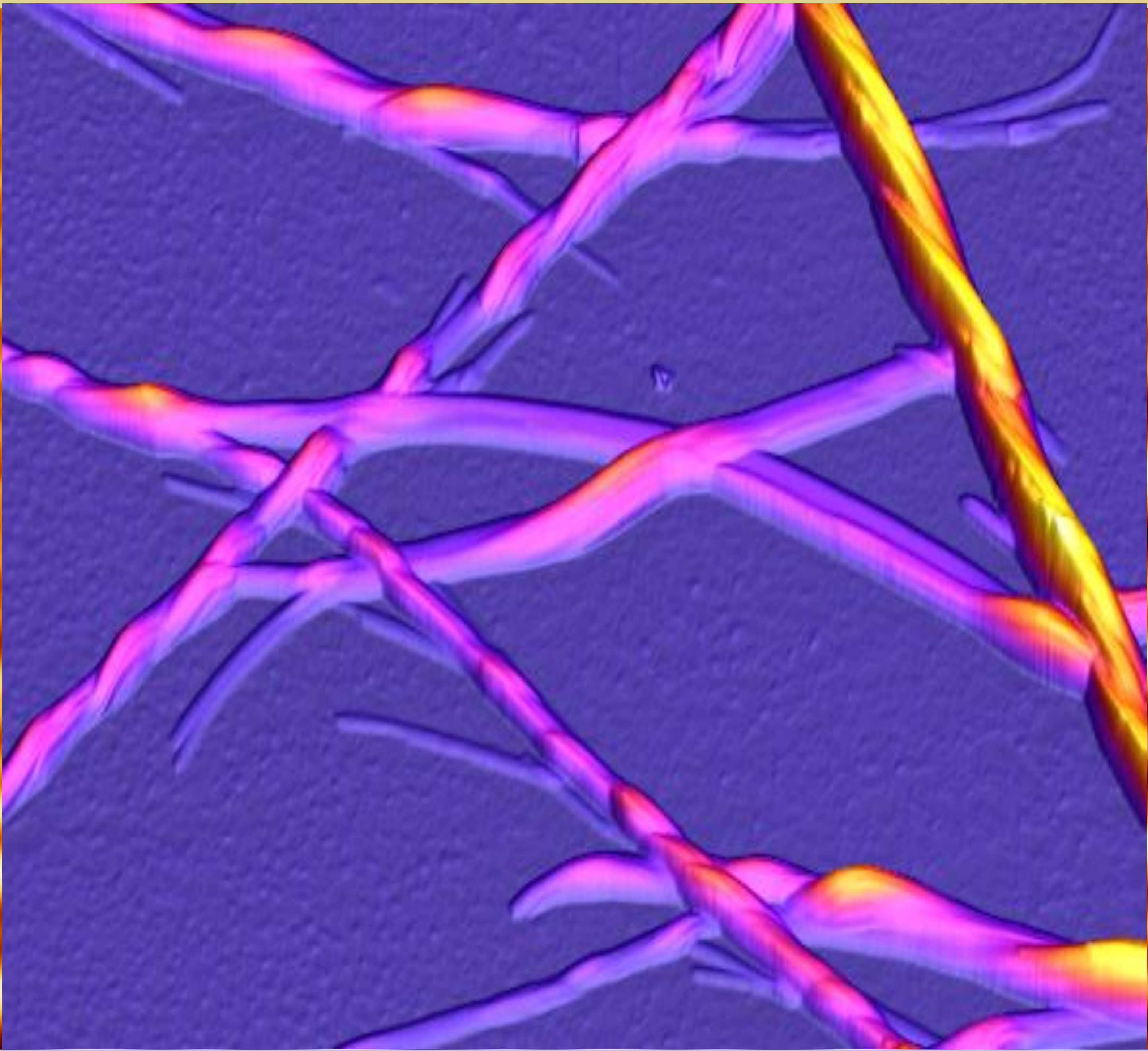

university of aveiro tema centre for mechanical technology and automation

Volume 5, Number 1 October 2023

Nanomaterials Science & Engineering

university of aveiro tema centre for mechanical technology and automation

Title
Nanomaterials Science & Engineering (NMS&E), Vol.1, No.5, 2023

Editors-in-Chief
Igor Bdikin
Paula Alexandrina de Aguiar Pereira Marques
Duncan Paul Fagg
Gil Alberto Batista Gonçalves

Editorial Board
Alexander Titov, Andrei Kovalevsky, António Manuel de Amaral Monteiro Ramos, António Manuel de Bastos Pereira, António Manuel Godinho Completo, Bagautdinov Bagautdin, Binay Kumar, Budhendra Singh, Cicero R. Cena, D. Pukazhselvan, Dmitry A. Kiselev, Dmitry Karpinsky, Eudes Borges de Araujo, Gil Gonçalves, Gonzalo Guillermo Otero Irurueta, Indrani Coondoo, João Paulo Davim Tavares da Silva, José Coutinho, Maciej Wojtas, Manoj Kumar Singh, Margarida Isabel Cabrita Marques Coelho, Maxim Silibin, Münir Tasdemir, Neeraj Panwar, Nikolai Sobolev, Oleksandr Tkach, Paula Celeste da Silva Ferreira, Philip Leduc, Radheshyam Rai, Sergey Bozhko, Svitlana Kopyl, Vincent Ball, Vítor António Ferreira da Costa, Vladimir Bystrov, Yuri Dekhtyar

Editorial Managers
Igor Bdikin
Gil Gonçalves
Raul Simões

Cover and Logo
Igor Bdikin (Phenylalanine microcrystals, AFM image, 5x5x0.2 μm^3)

Publisher
University of Aveiro

Support
Serviços de Biblioteca, Informação Documental e Museologia
Centre for Mechanical Technology & Automation (TEMA)
Mechanical Engineering Department
University of Aveiro

Copyright Information
All work licensed under Creative Commons Attribution License that allows others to share the work with an acknowledgement of the work's authorship and initial publication in this journal. Copyrights to illustrations published in the journal remain with their current copyright holders. It is the author's responsibility to obtain permission to quote from copyright sources.

Mailing Address
Department of Mechanical Engineering
University of Aveiro
Aveiro 3810-193
Portugal
E-mail: bdikin@ua.pt

ISSN: 2184-7002

Nanomaterials Science & Engineering (NMS&E), Vol.5, No1, 2023

NANOMATERIALS SCIENCE & ENGINEERING
Vol. 5, No. 1, pp. 5-16 (2023)

RESEARCH ARTICLE

https://doi.org/10.34624/nmse.v5i1.32798

Comparison of the cyclic voltammetry of benzene-1,2-diol and benzene-1,2,3-triol and their ability to form films on the carbon working electrode after a single potential sweep cycle

Vincent Ball [1,2,*]

[1] *University of Strasbourg, Faculté de Chirurgie Dentaire, 8 rue Sainte Elizabeth, 67000 Strasbourg, France*
[2] *Institut National de la Santé et de la Recherche Médicale, Unité Mixte de Recherche 1121, 1 rue Eugène Boeckel, 67000 Strasbourg, France*
**Corresponding author, e-mail address: vball@unistra.fr*

Received 15 July 2023; accepted 31 August 2023; published online 20 October 2023

ABSTRACT

The deposition of thin films on electrode surfaces by methods like cyclic voltammetry (CV) or chronoamperometry was for a long time considered as a drawback owing to the passivation of the electrode and a subsequent reduction in its ability to allow for the determination of electroactive compounds. However, the easy deposition of thin films from electroactive molecules is also a surface functionalization method. In this article the ability of 1,2-dihydroxybenzene (catechol) and of 1,2,3-trihydroxybenzene (pyrogallol) to form films impermeable to potassium hexacyanoferrate after only one CV « deposition » cycle will be compared. The addition of an additional hydroxyl group on catechol improves the film forming ability in the potential sweep rate window between 1 and 100 mV.s^{-1}. The obtained data will be interpreted in terms of the reversible (mostly for catechol) versus irreversible nature (in the case of pyrogallol) of the « deposition » cycle.

1. INTRODUCTION

The formation of passivating films on electrodes upon potential cycling (as in cyclic voltammetry) or under potentiostatic regime (as in chronoamperometry) is often considered as a major drawback in electrochemical processes. For instance, the oxidation Br- and I- on platinum electrodes is inhibited in the presence of phenol which is oxidized and electropolymerized at the electrode surface [1]. However, the formation of electro or bioactive films from redox active monomers can also be considered as a major advantage to coat the conductive electrode material with a robust and conformal film for applications like in protection against corrosion [2] or as platforms for biosensing [3]. One non negligible advantage of electrodeposition is that the molecules not in contact with the electrode or already deposited film are not lost and can be re-used for further deposition whereas oxidation induced by a soluble oxidant leads to film deposition at the solid/liquid interface and to uncontrolled precipitation in solution. For instance, conductive films can be obtained by the electropolymerization of aniline [4], pyrrole [5] and mixtures of aniline and pyrrole [6]. Catecholamines like dopamine in deareated solutions [7-9] (at or near physiological pH), but also phenol [10, 11] and its derivatives like 1,2-dihydroxybenzene (catechol) [12-14], 1,2,3-trihydroxybenzene (pyrogallol) [15] yield conformal thin films upon electrodeposition. Interestingly, based on the effect

This work is licensed under a Creative Commons Attribution-NonCommercial 4.0 International License.

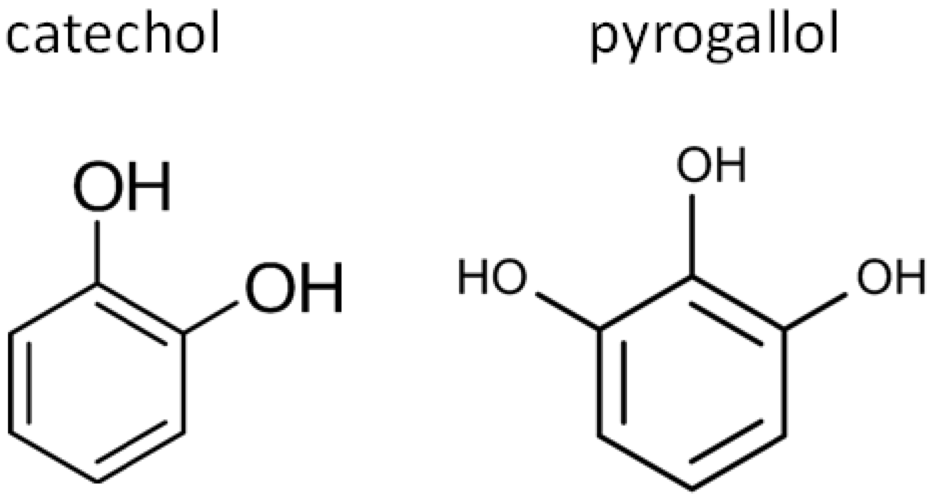

Scheme 1. Structure of the two investigated compounds.

of inductive and resonance effects, the electrodeposition of the three isomers of dihydroxybenzenes is markedly different with almost no film deposition on amorphous carbon electrodes (at pH = 5.0 in the presence of 50 mM sodium acetate buffer) from 1,4-dihydroxybenzene containing solutions [16]. Comparing 1,3-dihydroxybenzene (resorcinol) with 1,2-dihydroxybenzene (catechol), the former undergoes oxidation at more anodic potentials (on an amorphous carbon electrode versus an Ag/AgCl reference electrode) than the later but passivates the electrode after only one CV cycle at 20 mV/s, whereas catechol requires at least 5 CV cycles in the same conditions to reach electrode passivation [16]. The same findings have been made for meta substituted phenol and aniline [17]. The oxidation pathways of other meta substituted phenols have also been investigated [18-20]. Even if major research efforts have been devoted to the mechanisms [18-20] able to explain the oxidation-reduction of such molecules and their subsequent chemical reactivity, much less attention has been given on the influence of small structural or compositional variations on the film forming ability of phenol derivatives.

In such a context, the major aim of this investigation is to compare the electrodeposition by CV of catechol and of pyrogallol (scheme 1) as function of the potential sweep rate at a constant pH equal to 5.0. This investigation complements a previous one [15] in the sense that electrodeposition will be performed in broad potential rate range from 1 to 100 mV.s^{-1}. Both compounds are compared for their electron transfer coefficient to the electrode and in their ability to yield thin films impermeable to a redox probe as the negatively charged hexacyanoferrate anion after only one CV cycle performed at different potential sweep rates. The more impermeable the films are after only one potential sweep cycle, the better is the film forming ability of the investigated compound. This trend will also be confirmed by means of electrochemical impedance spectroscopy.

2. MATERIALS AND METHODS

All the required chemicals were used as purchased without further purification: catechol (ref. C9510, Sigma-Aldrich), pyrogallol (ref. P0381, Sigma) and potassium hexacyanoferrate (II) trihydrate (ref P9387).

The aqueous solutions were made from ultrapure and deionized water (ρ=18.2 MΩ.cm, Direct-Q®3UV, Millipore). The solutions of the electroactive molecules were prepared at 9.0 x 10^{-3} M whatever the tested compound just before the electrochemical deposition. The supporting electrolyte was 50 mM sodium acetate (ref. 9023841 from Merck) buffer at pH 5.0. The pH was adjusted with concentrated hydrochloric acid (ref. 403871 from Carlo Erba) and monitored with a calibrated pH meter (pH50 from VioLab, France). No care was taken to degas the used solutions, and therefore the electrochemical processes were investigated at potentials above -0.5 V vs the Ag/AgCl reference electrode.

The electrochemical deposition was performed with a PGSTAT204 potentiostat (Metrohm France) in a three electrode cell configuration using an amorphous carbon disk 2 mm in diameter (ref. CHI 104 from CHInstruments, Austin, Texas) as the working electrode, a Pt wire as the counter electrode (ref. CHI 115) and Ag/AgCl (ref. CHI 111) as the reference electrode. The device was controlled with the Nova 2.1.6 software (Metrohm). The working electrode was freshly polished on a SiC cloth, and then with two alumina slurries (1 and 0.1 µm, from Escil, Villeurbanne, France) before sonication in two water baths during 2 min. The surface state of the electrode was controlled by performing a CV scan between -0.5 and +1.0 V vs Ag/AgCl at a potential sweep rate of 100 mV.s^{-1} in the presence of 1mM potassium hexacyanoferrate. The polished electrode was used for electrodeposition provided the oxidation and reduction peaks were separated by less than 80 mV (the theoretical value being 59 mV for a reversible one electron oxidation-reduction process [21]). For each investigated molecule (Scheme 1) the potential was swept between -0.5 and +1.0 V versus Ag/AgCl at potential seep rates changing from 1 to 100 mV.s^{-1}. The permeability with respect to hexacyanoferrate of the deposited coating after only one "deposition cycle" (in the presence of either catechol or pyrogallol) was investigated in the following manner: after the "deposition" cycle the electrode was rinsed with sodium acetate buffer and subjected to 1 CV cycle in the presence of this buffer between -0.5 and +1.0 V versus Ag/AgCl at a potential sweep rate of 100 mV.s^{-1}. The same experiment was then reiterated in the same buffer but in the presence of 1 mM potassium hexacyanoferrate. The oxidation peak potential was identified and located using the Nova 2.1.6 software. The oxidation current at this potential was measured and the current measured at the same potential but in the absence of the redox probe was subtracted from it. This difference corresponds to the faradic oxidation current of the hexacyanoferrate anion: I_{film}. This current was compared to the faradic current of the redox probe on the pristine and polished electrode: Ielec. The relative permeability after one CV deposition cycle is hence quantified by:

$$Relative\ permeability = \frac{I_{film}}{I_{elec}} x100 \qquad (1)$$

A relative permeability of 0% corresponds to a totally impermeable and hence conformal film whereas a relative permeability close to 100 % corresponds to the absence of film deposition or to extremely porous films.

Electrochemical impedance spectra have been acquired on the films deposited after one CV scan at 50 mV/s in the presence of sodium acetate buffer containing 1 mM $K_4Fe(CN)_6$. The potential was

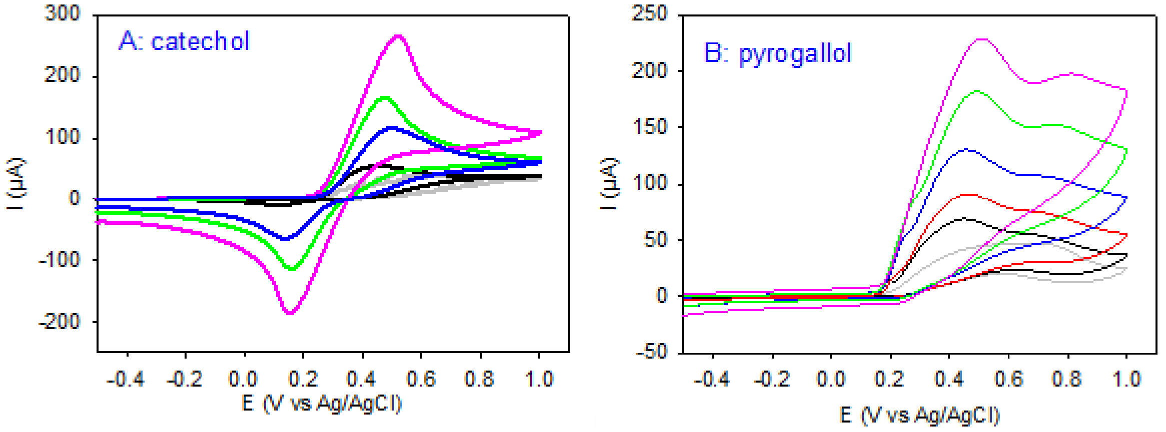

Figure 1. CV of catechol (panel A) and pyrogallol (panel B) at different potential sweep rates: (gray line—): 1 mV.s^{-1}, (gray dashed line- - -): 2 mV.s$^{-1,}$ (black line —): 5 mV.s^{-1}, (red line—): 10 mV.s^{-1}, (blue line —): 20 mV.s^{-1}, (green line —): 50 mV.s^{-1}, (purple line—): 100 mV.s^{-1}.

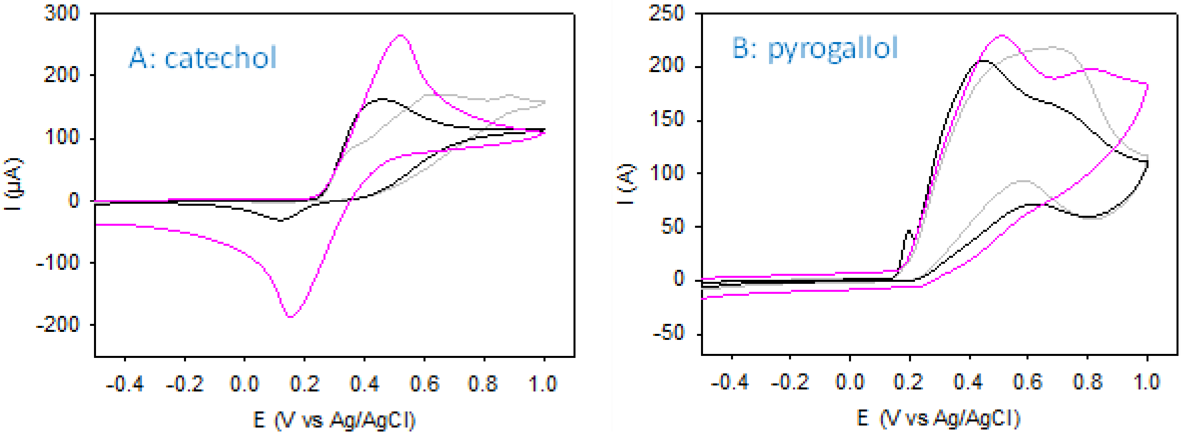

Figure 2: Detail of some CVs of catechol (panel A) and pyrogallol (panel B) performed at (—, gray line): 1 mV.s^{-1}, (—, black line): 5 mV.s^{-1} and (—, purple line); 100 mV.s^{-1}. The CVs performed at 1 and 5 mV^{-1} have been multiplied by 4.61 (ln100) and by 3.00 (ln 20) respectively as explained in the main text.

swept around the oxidation peak potential of $K_4Fe(CN)_6$ on the pristine electrode with an AC modulation of 5 mV in the frequency range from 10^5 to 10^{-2} Hz. 12 measurements were done per frequency decade. The data were fitted with the eisanalyser software (available on the internet for free).

3. RESULTS AND DISCUSSIONS

The CVs of catechol, pyrogallol, solubilized at 9 x 10^{-3} mol.L^{-1} and in the presence of 50 mM sodium acetate buffer (*pH*=5.0) on a polished amorphous carbon electrode have been recorded at different potential sweep rates between -0.5 and 1.0 V vs Ag/AgCl (Figure 1). This potential window was selected because the reduction wave of dissolved oxygen would be apparent below -0.5 V vs Ag/AgCl in non de-gased solutions as those used in this study. It appears that the oxidation wave of the two investigated compounds starts around +0.2 V vs Ag/AgCl and that the oxidation peaks are markedly influenced by the potential sweep rate as expected for either reversible or irreversible electrochemical processes [22]. In the case of pyrogallol, the CV is of irreversible nature, with no measurable reduction wave whatever the potential sweep rate. Hence, pyrogallol displays a markedly different behavior than catechol which CV displays a pronounced reversible character the more so the potential sweep rate is high. However, the CV of catechol becomes also irreversible, with no detectable reduction wave, at potential sweep rates lower than 5 mV.s^{-1} (Figure 1A). As another interesting observation, the first oxidation peak of pyrogallol is followed by a second one at potential sweep rates higher than 10 mV.s^{-1} as in other investigations but at a different electrode and in the presence of another electrolyte [22]. The appearance of this second peak may be related to a high reactivity of the first oxidation product of pyrogallol (a radical) allowing the occurrence of a second oxidation wave at high potential sweep rates, where the first oxidation product has no time to rearrange and form chemical bonds with neighboring pyrogallol molecules in the same oxidation state. However, at low potential sweep rates those radical intermediates have time to undergo some coupling with other molecules and loose hence their redox behavior, explaining the presence of only one redox wave at low potential sweep rates. Catechol displays a unique oxidation peak at those high potential sweep rates. However, the opposite holds true at low potential sweep rates. To emphasize the effect of the potential sweep rate, some typical CVs are plotted with the current multiplied by ln(100/v) because the highest potential sweep rate was equal to 100 mV.s^{-1}. In this representation catechol (Figure 2A) displays two additional oxidation peaks (not apparent in Figure 1 because of the representation mode) at low potential sweep rates at potentials around +0.6 and +0.8 V vs Ag/AgCl. They are still present at 2 mV.s^{-1} (data not shown)

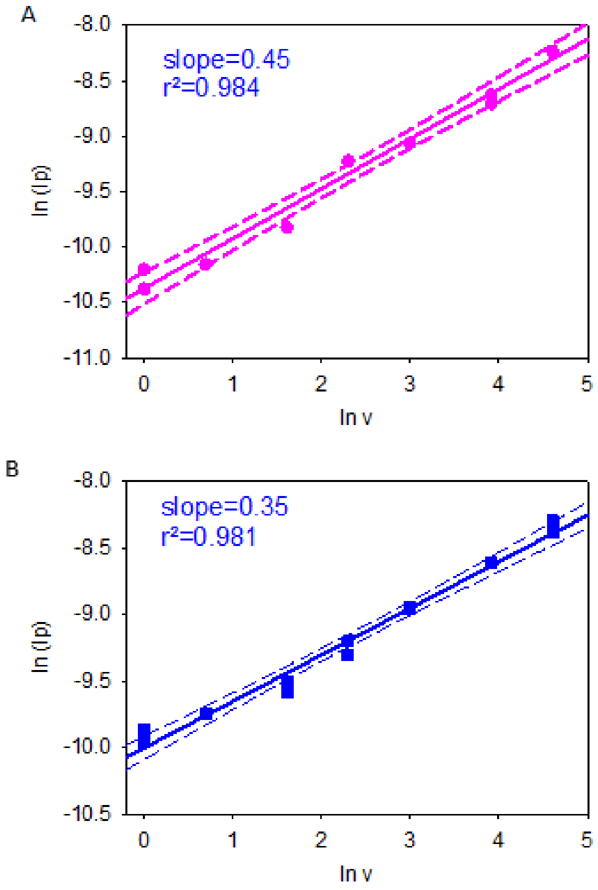

Figure 3: Evolution of the maximal oxidation current as a function of *lnV f*or the two investigated molecules, panel A: catechol and panel B: pyrogallol. The full and dotted lines correspond to a linear regression to the data and the limit of the 95 % confidence interval respectively. Each point corresponds to an independent experiment. The slopes of the curves and the linear regression coefficients are given in the insets.

but are not observed anymore when the CV is performed at 5 mV.s^{-1} (Figure 2A).

When considering the evolution of the mean oxidation peak current as a function of the potential sweep rate, no marked difference between catechol and pyrogallol appears whatever the potential sweep rate. The peak current should scale with v$^{1/2}$ when the electrochemical process is limited by diffusion to the electrode [21]. To confirm this the I_p vs V curve was plotted on a double logarithmic scale, yielding to slopes close to 0.5 as expected. However, in the case of pyrogallol the obtained slope of the $ln(I_{pa})$ versus lnV curve has a smaller slope than the corresponding curve for catechol. There is no available explanation for this qualitative finding at the moment. However, it seems robust owing to the number of performed experiments: 9 for catechol and for 11 pyrogallol (Figure 3).

However, a significant deviation from the theoretical behavior becomes pronounced when the main oxidation peak potential is plotted against the logarithm of the potential sweep rate (Figure 4). For an irreversible electron transfer, which is the case for pyrogallol at all investigated potential sweep rates and for catechol below 5 mV.s^{-1}, the following relationship is expected to be satisfied [22, 23]:

$$E_{p,a} = b + \left(\frac{RT}{2aF}\right).lnv \tag{2}$$

where $E_{p,a}$, R, T and v are the anodic peak potential, the universal gas constant, the temperature and the potential sweep rate

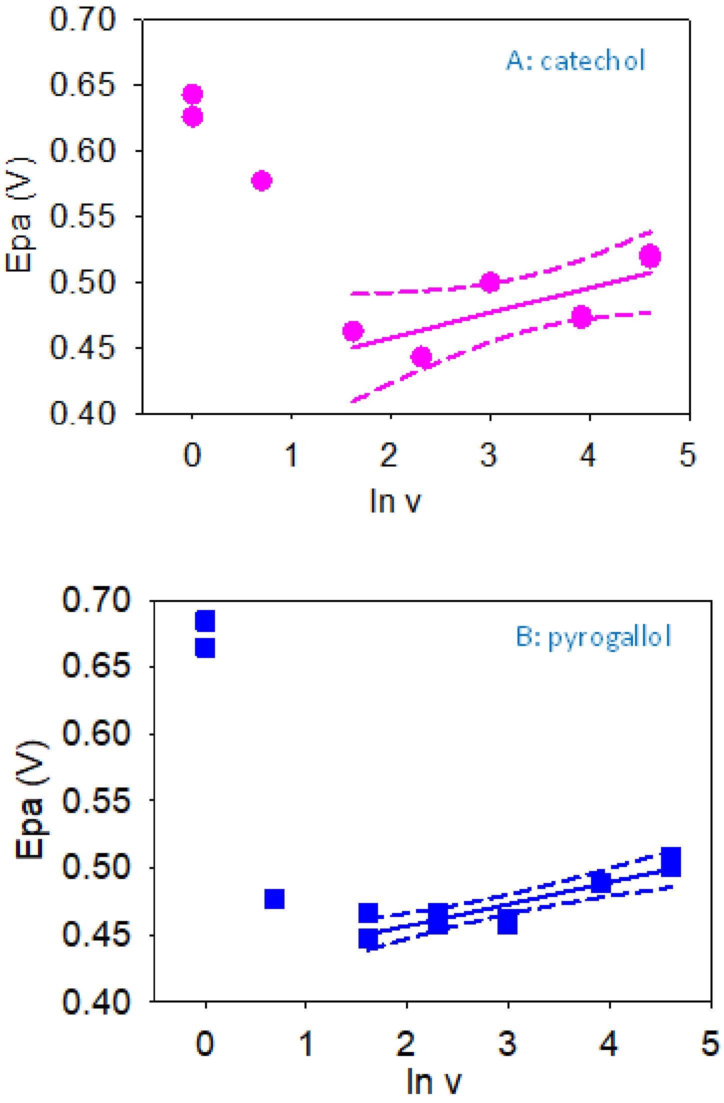

Figure 4: Evolution of the oxidation peak potential (at the first CV scan) as a function of the logarithm of the potential sweep rate. Purple disks and lines: catechol (panel A), blue squares and lines: pyrocatechol (panel B). The full lines correspond to a linear regression to the experimental data for potential sweep rates larger than 5 mV.s^{-1}. The dashed lines correspond to the limits of the 95 % confidence interval. Each point corresponds to an independent experiment.

respectively. *b* is a constant and *a* is the anodic electron transfer coefficient (sometimes represented by βn_β in the literature [22]). The fit of the equation (2) to the experimental data is satisfactory (Table 1) provided the sweep rate is higher than 5 mV.s^{-1} (Table 1) and this allows to provide an estimate of the value of the anodic electron transfer coefficient. But, both for catechol and pyrogallol, a clear change in the E_{pa} vs ln V regime is observed below this critical scan rate of 5 mV.s^{-1} (Figure 4). The quality of the fit of equation (2) to the experimental data is less good than the fit obtained for the lnI_{pa} versus lnV curves (Figure 3). This can be easily explained by the nature of the measurement itself: a current (Figure 3) and a potential (Figure 4). The potentials are measured versus a reference electrode (here Ag/AgCl) which is very stable, but the electrodes are polished and sonicated (see Materials and Methods) before every measurement and this slightly changes the peak potential values by a few mV. A measurement sequence starts with a CV cycle in a solution containing the reversible $Fe(CN)_6^{3-}$ / $Fe(CN)_6^{4-}$ redox probe [21]. This experiment is aimed to check the cleanliness of the electrode. It appears however that the oxidation potential peak during

Table 1 : Values of the slopes of the anodic peak potential versus the logarithm of the potential sweep rate (Figure 4) for catechol and pyrogallol and the corresponding anodic electron transfer coefficients calculated according to equation (2).

compound	Slope of the E_{pa} vs lnV curve (for $V \geq 5$ $mV.s^{-1}$)	r^2	anodic electron transfer coefficien – *a* in equation (2)
Catechol	0.019	0.66	0.68
pyrogallol	0.016	0.79	0.80

the oxidation of $Fe(CN)_6^{4-}$ changes in a 20 mV interval from one experiment to the other. This largely explains the pretty large variations observed in Figure 4 (and absent in the current measurements, Figure 3). These variations may not only originate from the electrode cleaning process but also from slight changes in the relative position of the electrodes in the electrochemical cell inducing some small changes in the solution resistance and hence some small potential changes.

Nevertheless, the slopes of the obtained curves and hence the calculated electron transfer coefficients (Table 1) are similar for catechol and pyrogallol. This implies that the first oxidation event of both molecules is probably the same at sufficiently high potential sweep rates ($V \geq 5$ $mV.s^{-1}$). It has to be noted that the electron transfer coefficient of pyrogallol on an amorphous carbon electrode and at *pH* = 5.0 (this investigation) is significantly higher than the values obtained on a Pt working electrode in the presence of 0.5 M H_2SO_4 [22]. Indeed, in these conditions two oxydation peaks are observed for pyrogallol one at around + 0.45 V and the second at around +0.9 V versus the saturated calomel electrode [22]. Since both the nature of the working electrode as well as the supporting buffer changed, it is not easy to compare the electron tranfer coefficient of pyrogallol obtained in the present investigation with the value reported in [22]. Nevertheless the value reported herein (*a*=0.80) is about twice the value

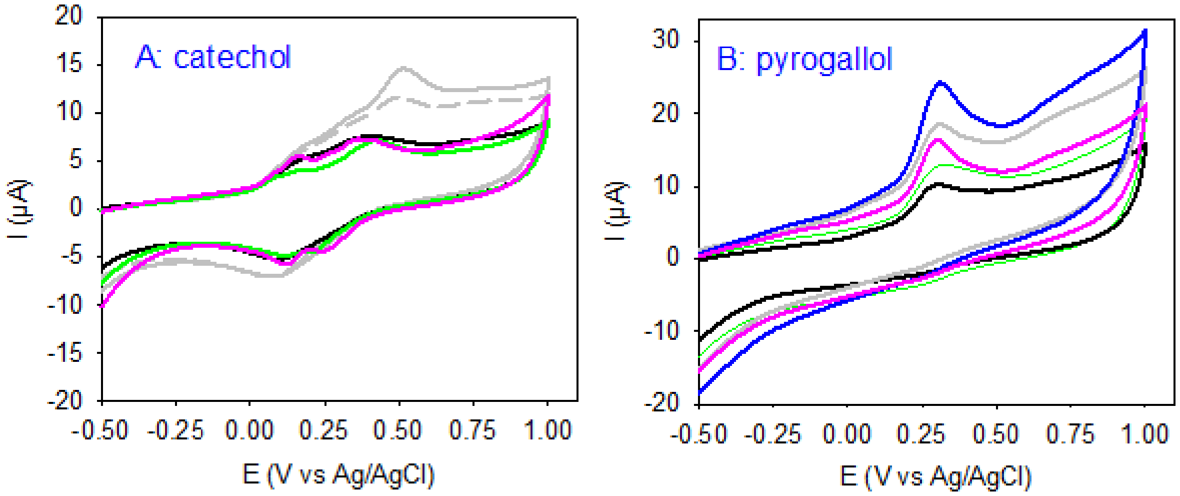

Figure 5: Capacitive curves acquired (at a potential sweep rate of 100 $mV.s^{-1}$) for catechol (panel A) and pyrogallol (panel B) films obtained after 1 CV cycle performed at different scan rates: (gray line —): 1 $mV.s^{-1}$, (gray dashed line - -): 2 $mV.s^{-1}$, (black line —): 5 $mV.s^{-1}$, (red line —): 10 $mV.s^{-1}$, (blue line —): 20 $mV.s^{-1}$, (green line —): 50 $mV.s^{-1}$, (purple line —): 100 $mV.s^{-1}$.

obtained on Pt for the corresponding peak (*a*=0.43) [22].

The most interesting, and intruiging finding of the present investigation, is the change in the peak potential variation with the potential sweep rate below about 5 mV.s^{-1} (Figure 4). This is totally unexpected with respect to the theory of electron transfer (equation (2)) but is related to the appearance of different oxidation peaks at those low potential sweep rates (Figure 2). At the present state of knowledge one can thus just make the assumption that the mechanism of catechol/pyrogallol oxidation and the subsequent non electrochemical processes they undergo, as radical coupling followed by polymerisation [18, 19, 22] are radically different when more time is allowed for the radical species to react, namely at low potential sweep rates. The effect is anyway higher for catechol than for pyrogallol, because the former keeps some partial reversible character (manifested by the appearance of a reduction current at high potential sweep rates) whereas the later displays irreversible CV curves (with no measurable faradic reduction current) in the whole potential sweep rate window. The strong influence of the potential sweep rate on the electron transfer to the electrode and the subsequent non electrochemical processes should also manisfest in a change in the composition and structure of the deposited coatings. To asses this point in a qualitative manner, CV measurements of the electrodes after the first « deposition » cycle in the presence of catechol or pyrogallol were done at 100 mV.s^{-1} in the presence of sodium acetate buffer only (without additional added redox probe) (Figure 5). The CV curves (displayed after the CV in the presence of catechol or pyrogallol have been performed between 1 and 100 mV.s^{-1}) display an oxydation wave and a reduction wave in the case of catechol, whereas no reduction wave is measured in the case of pyrogallol. But the measurement of an oxydation wave for both molecules is a proof that an electroactive film has been deposited. These films are electroactive because they can be oxidized (and reduced in the case of catechol). Catechol based films distinguish from the pyrogallol ones not only by the partially reversible character of the measured CV but also by the following points:

(i) The oxidation wave at potential sweep rates higher than about 5 mV.s^{-1} is made of two peaks.

(ii) A new anodically shifted oxidation peak is detected at about +0.5 V versus Ag/AgCl.

Observation (ii) may be related to the upshifted oxidation potential peak measured during the CVs performed with catechol solutions at low potential sweep rates (Figure 2 and Figure 4) and suggests that the reaction product obtained from catechol is totally different when the deposition is performed at

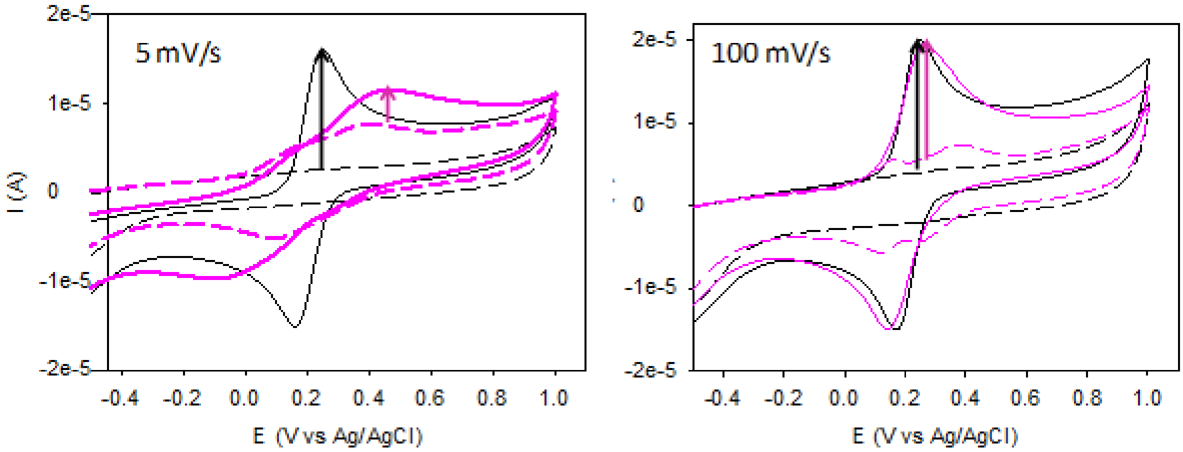

Figure 6: Some representative capacitive curves (dashed lines) and oxidation-reduction of hexacyanoferrate (full lines) before (black color) and after (purple color) 1 deposition CV cycle performed at either 5 or 100 mV.s^{-1} as indicated above the curves. The black and purple arrows indicate the faradic current due to the oxidation of hexacyanoferrate anions on the polished electrode and on the electrode after 1 CV cycle respectively, in the presence of catechol (1 mg.mL^{-1} in 50 mM sodium acetate buffer at *pH* = 5.0).

a sufficiently low potential sweep rate. In the case of pyrogallol the deposited species seem to be relatively independent on the potential sweep rate during the deposition CV cycle (Figure 5).

Spectroscopic and structural investigations, like infrared, Raman spectroscopies and transmission electron microscopy need to be performed on the obtained coatings and will be the subject of upcoming investigations. Those kinds of film characterizations have already been done for catechol based films deposited at 20 mV.s^{-1} in the same sodium acetate buffer on amorphous carbon electrodes as a function of an increasing number of potential sweep cycles [14]. It was found that the obtained films, obtained in conditions where the CV displays a partially reversible character, are close to graphene oxide. One important question will be to know if this structure is conserved or lost when the deposition of catechol is performed at potential sweep rates below the critical 5 mV.s^{-1} value.

Figure 5 shows that an electroactive deposit is obtained from catechol or pyrogallol containing solutions whatever the potential sweep rate chosen during the CV. It is of interest to investigate if these coatings, obtained after a single CV scan, are conformal without defects, allowing for a redox probe to reach the electrode and to be oxidized or reduced there. To that aim, in every experiment performed, after the CV scan performed in buffer without redox probe (the data are displayed in Figure 5), a new CV scan at 100 mV.s^{-1} but in the presence of 1 mM potassium hexacyanoferrate was performed (Figure 6).

When the deposition was performed at 1 mV.s^{-1} no faradic current in addition to that measured on the film but without redox probe was found. When the deposition was performed above 5 mV.s^{-1} an additional faradic current was found but the oxidation peak potential was anodically shifted in an almost constant amount in the case of pyrogallol but with a decreasing shift in the case of catechol (see the purple curves in Figure 6). When the deposition cycle is performed at 100 mV.s^{-1}, almost no current reduction and almost no peak potential shift is obtained with respect to the polished electrode before the deposition (compare the full black and the full purple curve in Figure 6B) even if some material has been deposited on the electrode (purple dashed line in Figure 6B).

These data, comparing the faradic current on the film and on the polished electrode with the currents measured in the absence of $Fe(CN)_6^{4-}$ (arrows in Figure 6) allow to calculate the remaining permeability of the film towards the redox probe according to equation (1).

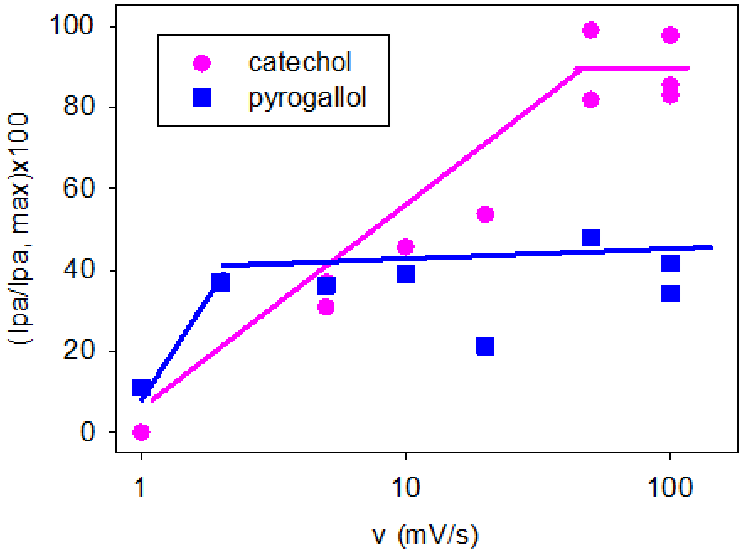

Figure 7: Permeability change as a function of the scan rate for catechol and pyrogallol (as indicated in the inset) after only one CV “deposition” cycle. The purple line is aimed to guide the eye in the case of catechol based films whereas the blue line is aimed to guide the eye in the case of the films made from pyrogallol.

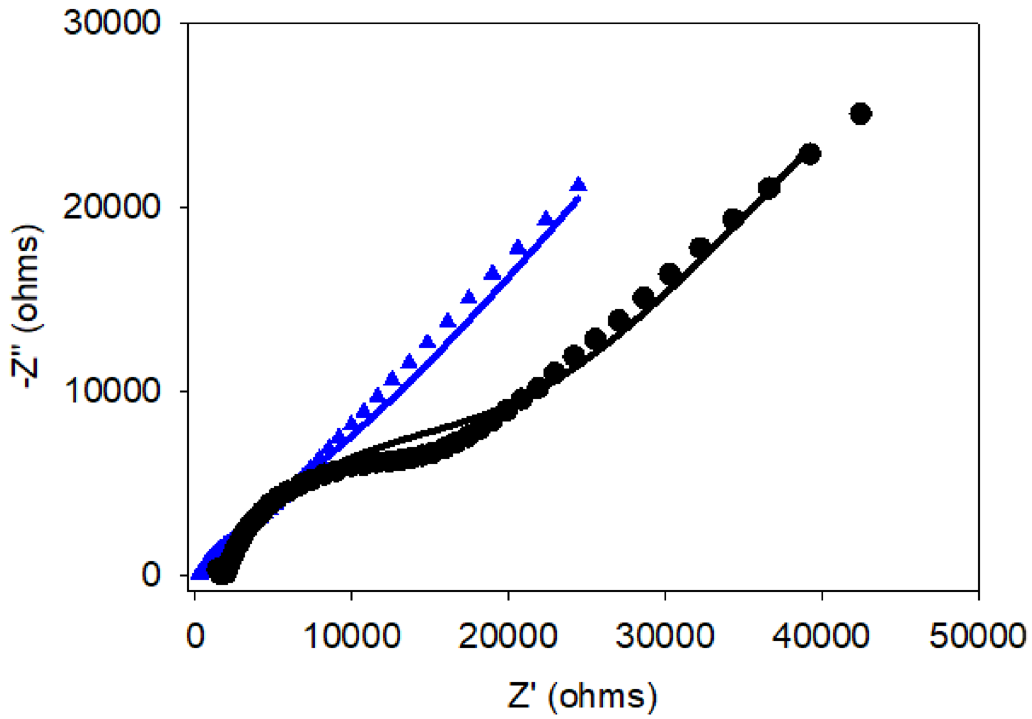

Figure 8: Nyquist plots of the electrochemical impedance spectra of pyrogallol (black circles) and catechol (blue triangles) based coatings obtained after 1 CV cycle at a potential sweep rate of 50 mV/s. The full lines correspond to the fit of a model corresponding to the Randless equivalent circuit (Scheme 2).

It appears that the catechol and pyrogallol based films are fully impermeable to the used (negatively charged) redox probe only when the deposition potential sweep rate is equal to 1 mV.s^{-1}. At all the higher potential sweep rates, the films display some permeability and are either porous or non conformal. But a marked difference is observed between the catechol and pyrogallol based deposits : in the case of catechol the permeability gradually increases to 100 % (hence very few material deposition) whereas the potential sweep rate during the deposition cycle has almost no influence on the permeability to hexacyanoferrate for pyrogallol based films when the potential sweep

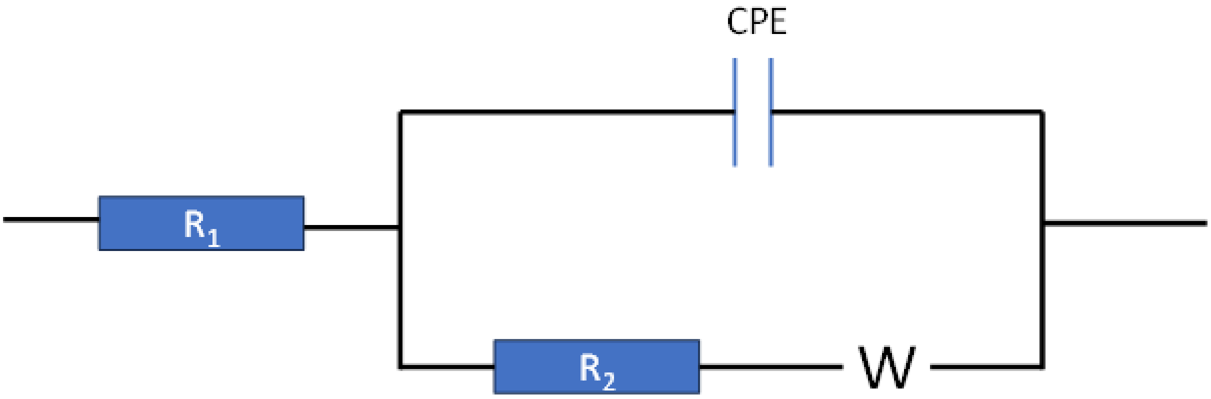

Scheme 2: Randless equivalent circuit used for the modelization of the electrochemical impedance spectra shown in Figure 8: R_1, R_2, *CPE* and *W* represent the solution resistance, the resistance of the film to the electron transfer, the constant phase element and the Warburg impedance respectively [23].

Table 2: Fitting parameter values of the Randless equivalent circuit to the electrochemical impedance spectra of the catechol and pyrogallol based films obtained after CV induced deposition (one cycle at 50 mV/s).

Compound	R_1 ($\Omega.cm^2$)	R_2 ($\Omega.cm^2$)	CPE ($\mu F.cm^{-2}$)	n	W ($\Omega.cm^2$)
Catechol	1450 ±80	$(1.05 \pm 0.10)x\ 10^4$	7±3	0.59 ± 0.02	2300 ± 400
Pyrogallol	1600±50	$(2.06 \pm 0.15)\ x\ 10^4$	16±1	0.66±0.01	6400 ± 900

rate exceeds 5 $mV.s^{-1}$. This points to a more efficient electrochemical deposition behavior by CV for pyrogallol when compared to catechol. It has to be noted that for both investigated molecules a completely imperable film (with respect to $Fe(CN)_6^{4-}$) can be obtained after a higher number of « deposition » CV cycles [13, 15]. But in the present investigation, it is shown that the impermeable state can be reached after only one « deposition » CV cycles for both compounds, hence in conditions where enough time is allowed between the onset of oxidation at about +0.2 V vs Ag/AgCl and the end of the CV cycle at -0.5 V vs Ag/AgCl. At 1 $mV.s^{-1}$ this time duration amounts to 2300 s whereas it amounts to only 23 s when the potential is sweeped at 100 $mV.s^{-1}$. During such a long time interval oxyidized and still absorbed molecules can diffuse on the surface and undergo some radical coupling to yield a conformal film.

To get more semi quantitative information about the electrochemical properties of the deposited films, namely their electrical conductivity, capacity and ionic transport properties related to their permeability (Figure 7) some electrochemical impedance spectroscopy experiments in the presence of 1 mM $K_4Fe(CN)_6$ were performed. Those electrochemical impedance spectra (Figure 8) could be fitted satisfactorily with the model corresponding to the Randless equivalent circuit (Scheme 2). It appeared that the pyrogallol based film displays a much larger value of the Warburg impedance (by a factor of almost 3, see Table 2) than the catechol based film. This strongly suggests that the hexacyanofferate anions have more difficulties to diffuse across the pyrogallol based film than catechol based one or that the former are less porous than the later. These data are consistent with the finding that the pyrogallol based films are much less permeable to the used redox probe (Figure 7) than their catechol based counterparts (after 1 CV cycles and at this particular potential sweep rate). Note that the electrochemical impedance spectra of the pyrogallol and catechol based films obtained after two CV cycles performed at 20 mV/s are given in Fig. 4 of [15]) and are coherent with the findings presented in this study: namely that the pyrogallol based coatings are less permeable to hexacyanoferrate anions than the catechol based coatings. The difference in permeability is just more pronounced after two CV (in ref. [15]) deposition cycle than after one cycle (herein).

In addition, the fit of the Randless equivalent circuit model to the data indicates that the pyrogallol based film displays a higher resistance to the electron transfer (by a factor of 2) and a higher capacitance (by a factor of 2 also) than the catechol based film. This could suggest that the pyrogallol based films are either thicker or more compact than their catechol counterparts. In the future, this assumption needs to be confirmed by imaging techniques like Atomic Force Microscopy. Anyway this property to yield films with low permeability to the used redox probe seems to be closely related to the shape of the CV curves (Figure 1 and 2). Important film deposition and significant or total permeability supression occurs only for irreversible CVs, i.e. without measurable faradic reduction current. In the case of pyrogallol, the « deposition » CV display an irreversible character at all the investigated potential sweep rates and a full or about 60 % permeability reduction. However in the case of catechol, the CV become irreversible only when the deposition is performed below 5 mV.s^{-1} (Figure 2A). At higher potential sweep rates, the reduction wave during the CV becomes more marked (Figures 1A and 2A) and the permeability of the deposit markedly increases (Figure 7).

4. CONCLUSIONS

This investigation was aimed to complement the previous one [15] aimed to compare film deposition on amorphous carbon electrodes and at *pH* = 5.0 from catechol and pyrogallol differing by the addition of an additional OH group on position 3 of phenol (Scheme 1). It appears that the CV of pyrogallol solutions are of an irreversible nature (without an observable reduction current) for potential sweep rates between 1 and 100 mV.s^{-1} as those of resorcinol [16] but the onset of oxidation occurring at much lower potentials in the case of pyrogallol (about +0.2 V vs Ag/AgCl) compared to resorcinol (about +0.7 V vs Ag/AgCl) [16]. However, the CVs of catechol containing solutions display a reduction peak of increasing intensity when the potential sweep rate is higher than about 5 mV.s^{-1} and become irreversible only below this critical potential rate value. The possibility to obtain films impermeable to hexacyanoferrate anions after only one "deposition" CV cycle is more efficient for pyrogallol than for catechol even if both molecules yield to impermeable films when the deposition is performed at 1 mV.s^{-1}. At the highest investigated potential sweep rate, the catechol based coatings are totally permeable to the used redox probe whereas the pyrogallol based coatings display a reduction of permeability close to 60 %. This investigation highlights, as the previous one on the same topic [15], that the addition of a third OH group on the meta position of catechol improves the film forming ability of the derivative. Further studies will be aimed to investigate the chemical composition and the structure of the pyrogallol based films at all the investigated potential sweep rates and to compare them with the catechol based coatings which are known to yield graphene oxide based films on amorphous carbon electrodes at a potential sweep rate of 20 mV.s^{-1} [14].

REFERENCES

[1] T. Bejerano, Ch. Forgacs, E. Gileadi, *Electronal. Chem. & Interf. Electrochem*. **27**, 69-79 (1970).
[2] G. Mengoli, M.M. Musiani, *Prog. Org. Coat*. **24**, 237-251 (1994).
[3] E. Wajs, N. Fernández, A. Fragoso, *Analyst* **141**, 3274-3279 (2016).
[4] Y.Z. Li, Y. Yi, W.F. Yang, X.Q. Liu, Y.Y. Li, W. Wang, *J. Electron. Mater*. **46**, 1324-1330 (2017).
[5] S.B. Saidman, M.E. Vela, *Thin Solid Films* **493**, 96-103 (2005).
[6] J.Q. Iroh, R. Rajagopalan, *Surf. Eng*. **16,** 481-486 (2000).
[7] F. Bernsmann, J.-C. Voegel, V. Ball, *Electrochim. Acta* **56**, 3914-3919 (2011).
[8] Y. Li, M. Liu, C. Xiang, Q. Xie, S. Yao, *Thin Solid Films* **497**, 270-278 (2006).
[9] S. Li, H. Wang, M. Young, F. Xu, G. Cheng, H. Cong, *Langmuir* **35**, 1119-1125 (2019).
[10] R. Lapuente, F. Cases, P. Garcès, E. Morallón, J.I. Vázquez. *J. Electroanal. Chem*. **451**, 163-171 (1998).
[11] M. Gattrell, D.W. Kirk, *J. Electrochem. Soc*. **139**, 2736-2744 (1992).
[12] Q. Lin, Q. Li, C. Batchelor-McAuley, R.G. Compton, *J. Phys. Chem. C* **119**, 1489-1495 (2015).
[13] V. Ball, *Colloids & Surf. A: Physicochem. Eng. Aspects* **518**, 109-115 (2017).
[14] N. Ortiz-Peña, D. Ihiawakrim, V. Ball, S. Stanescu, M. Rastei, C. Sanchez, D. Portehault, O. Ersen, *J. Phys. Chem. Lett*. **11**, 9117-9122 (2020).
[15] V. Ball, *J. Electroanal. Chem*. **909**, art. 116142 (2022).
[16] V. Ball, M.-L. Alfieri, K. Ziegler, Y. Arntz, M. d'Ischia, *Surfaces and Interfaces*. **20**, art.101841 2022)
[17] B. Kennedy, A. Glidle, V.J. Cunnane, *J. Electroanal. Chem*. **608**, 22-30 (2007).
[18] T.A. Enache, A.M. Oliveira-Brett, *J. Electroanal. Chem*. **655**, 9-16 (2011).
[19] K. Ngamchuea, B. Tharat, P. Hirunsit, S. Suthirakun, *RSC. Adv*. **10**, 28454-28463 (2020).
[20] M.R. Deakin, R. M. Wightman, *J. Electroanal. Chem*. **206**, 167-177 (1986).
[21] P.T. Kissinger, W.R. Heineman, *J. Chem. Educ*. **60**, 702-706 (1983).
[22] H. Nady, M. El-Rabiei, G.A. El Hafez, *Egypt. J. Pet*. **26**, 669-678 (2017).
[23]E. Gileadi, Physical Electrochemistry-Fundamentals, techniques and applications, chapter 15, Wiley-VCH, Weinheim (2011).

NANOMATERIALS SCIENCE & ENGINEERING
Vol. 5, No. 1, pp. 17-24 (2023)

RESEARCH ARTICLE

https://doi.org/10.34624/nmse.v5i1.33484

Local piezoelectric properties of Di-Leucine dipeptides nanotubes

Igor Bdikin [1, 2, *]

[1]*TEMA: Centre for Mechanical Technology and Automation, Department of Mechanical Engineering,*
University of Aveiro, Campus de Santiago, 3810-193 Aveiro, Portugal
[2]*LASI—Intelligent Systems Associate Laboratory, Guimarães, Portugal*
**Corresponding author, e-mail address: bdikin@ua.pt*

Received 13 September 2023; accepted 3 October 2023; published online 20 October 2023

ABSTRACT

Di-Leucine (LL) peptide nanotubes (PNTs) were grown. The local piezoelectric properties of LL PNTs were measured using atomic force microscopy. Using piezoresponse force microscopy the strong piezoelectric properties with d_{15} ~3.2 pm/V was found. The magnitude and distribution of the piezo response signal were analysed depending on the orientation of the tubes. Features of the charge distribution depending on the microstructure of LL PNTs were discovered by Kelvin Probe Force Microscopy.

1. INTRODUCTION

Di-peptides nanotubes (PNTs) have received much attention in the last decade because of their close relationship with life and the nanotube formation by various hydrophobic dipeptides and its structural properties were studied by many authors [1, 2]. These are materials absolutely corelated with biology (systhesis, physical and chemical properties, utilizations) and their have many potential applications in various broadening fields from medicine (as containers for medical, biosensors, etc [3-6]) to technology energy (harvesting), nanoelectronics [7], semiconducting nanostructures [8], colored surfaces [9], etc. Polypedide structure of PNTs is very close to polyt – DNR and RNR. So, PNTs are as well as genetic and tissue (protein) engineering. Tubular structures can be constructed with cyclic di-, tri-, tetra-, hexa-, octa-, and decapeptides with various amino acid sequences, enantiomers, and functionalized side chains and can be applied for antiviral and antibacterial drugs, drug delivery and gene delivery vectors, organic electronic devices, and ionic or molecular channels [10]. From another side known PNTs nanotubes structures have crystal structure what is possible to do analysis from material science point as conductor, semiconductor and possible to do controlled microstructure different blocks and elements for electronics [11], for example, dipeptides DiHpa, DiApp, and DiAph [12]. Hierarchical self-assembly Phe peptide blocks can form nano and micro-structures sized assemblies [13]. Self-assembly di-para-fluoro-Phe, di-pentafluoro-Phe, di-para-iodo-Phe, di-4-phenyl-Phe, di-para-nitro-Phe well-ordered nanostructures [14] and morphological twist in Phe-Phe dipeptide conjugates [15] were obtained. Self-assembly of Fc-coupled diphenylalanine (Phe-Phe, FF) and then used as supporting matrix for immobilization of glucose oxidase (GOx) were synthesized [16]. Self-organization Asp-Phe PNTs, Tyr-Ala (YA) and Asp-Phe [17], metal-mediated modification of spherical soft assemblies Phe–Phe dipeptide [18] are known. The peptide H-Phe(4-azido)- Phe(4-azido)-OH self-assembled into porous spherical structures, whereas the peptides H-Phe(4-azido)-Phe-OH and H-Phe-Phe (4-azido)-OH [19] was describes too. Ile-Gln-Ser-Pro-His-Phe-Phe (IQSPHFF) identified and found to undergo self-assembly into microparticles in solution [20]. Boc-Ile-Ile-OMe, Boc-Phe-Phe-Phe-Ile-Ile-OMe and Boc-Trp-Ile-Ile-OMe showed nanotubular structures [21]. Self-

This work is licensed under a Creative Commons Attribution-NonCommercial 4.0 International License.

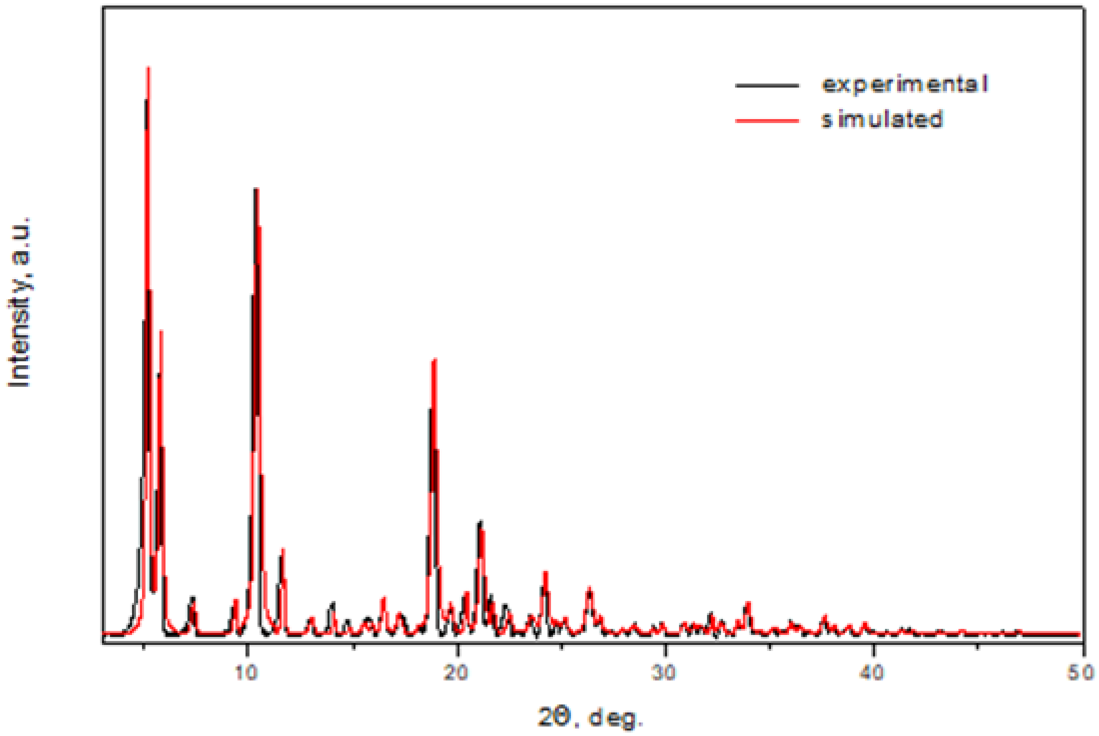

Figure 1. Experimental and simulated XRD patterns of Leucine dipeptide PNTs.

assembly of aromatic CDP (Phe-Phe) into fibre bundles with 1–2 mm thick and several millimetres long is described [22]. Using zwitterionic Phe-Phe dipeptides and straightforward experimental procedures tubular and vesicular dipeptide structures [23], oriented self-assembly dipeptides films [24] have been grown.

Piezoelectricity is the ability of no centrosymmetric crystals to produce mechanical stress/strain under electric field or charge under mechanical stress. This fundamental property has long been used in numerous devices microelectromechanical systems (MEMS): such as acoustic transducers, sensors and actuators, piezoelectric motors, rf resonators, SAW filters, micro energy generators (energy harvesting). To date, one of the most popular energy harvesting or piezoelectric sensor materials is lead zirconium titanate (PZT) because of its high piezoelectric constant and electromechanical coupling factor. However, the critical issues currently limiting its wide applications lie in its fragility and environmental hazardous element (lead). To address these problems, much effort has been expended on the piezoelectric organic compounds and their composites (PNTs) [25]. Strong piezoelectric activity in glycine and diphenylalanine nanotubes (FF PNTs) holds a great promise for using piezoeffect in such applications was discovered [26-29].

We investigated the electromechanical properties of new PNTs: Di-Leucine (LL).

Table 1. Crystal data of Leucine dipeptide.

a, Å	b, Å	c, Å	α	β	γ	V, Å^3
33.087	16.999	6.062	90°	90°	90°	3409.55

Table 2. Reflection indices, d_{hkl} values and relative peak intensities in the simulated XRD patterns for XRD of Leucine dipeptide on Fig. 1.

No.	Pos. [°2Th.]	h	k	l	d-spacing [Å]	Rel. Int. [%]
1	5.1829	2	0	0	17.05077	100
2	5.7972	1	1	0	15.24548	52.59
3	7.3749	2	1	0	11.98719	5.72
4	9.3783	3	1	0	9.43046	6.22
5	10.4337	4	0	0	8.4788	78.96
6	11.6477	2	2	0	7.59762	15.29
7	13.0209	3	2	0	6.79934	3.07
8	14.0963	5	1	0	6.28292	3.92
9	14.8404	1	0	1	5.96952	1.15
10	15.5556	2	0	1	5.69666	2.11
11	15.9248	1	3	0	5.56539	1.86
12	16.4674	2	3	0	5.38321	6.69
13	17.2118	3	1	1	5.15204	3.63
14	18.0761	1	2	1	4.90761	0.9
15	18.8833	6	2	0	4.69959	49.52
16	19.6784	5	0	1	4.51148	4.6
17	20.437	5	3	0	4.3457	7.87
18	21.1547	7	2	0	4.19985	18.99
19	21.6979	8	1	0	4.09592	5.39
20	22.4735	3	4	0	3.95629	3.69
21	22.9621	3	3	1	3.8732	0.32
22	23.5433	7	0	1	3.77889	3.08
23	24.2113	7	3	0	3.67613	11.31
24	24.7465	5	4	0	3.59782	1.93
25	25.1491	5	3	1	3.54113	2.82
26	26.3298	1	5	0	3.38495	8.62
27	26.8473	10	1	0	3.32087	3.24
28	27.2507	3	5	0	3.27262	0.63
29	27.9538	7	4	0	3.19188	0.89
30	28.4699	9	3	0	3.13518	1.73
31	29.3714	5	5	0	3.04098	0.96
32	29.8293	9	2	1	2.99533	1.89
33	30.8676	11	2	0	2.8969	2.12
34	31.362	4	0	2	2.85235	1.85
35	31.6858	7	4	1	2.82393	1.75
36	32.1921	12	1	0	2.78067	4.25
37	32.6298	11	0	1	2.74436	2.2
38	33.4582	12	2	0	2.67829	2.59
39	33.9177	2	3	2	2.64305	6.09
40	34.4937	3	3	2	2.60022	0.44
41	35.192	4	3	2	2.55021	1.21
42	35.9805	11	4	0	2.49611	2.27
43	36.4499	8	0	2	2.46504	1.39
44	36.7902	2	4	2	2.44302	0.5
45	37.5935	14	1	0	2.39264	3.48
46	38.0678	13	3	0	2.36391	1.39
47	38.7637	14	2	0	2.32306	1.54
48	39.5188	11	5	0	2.2804	1.95
49	40.5768	14	3	0	2.22335	0.31
50	41.2749	4	5	2	2.18734	1
51	41.8341	11	0	2	2.15939	0.62
52	43.0997	16	1	0	2.09887	0.46
53	44.168	7	5	2	2.05055	0.74
54	46.1086	0	2	3	1.96867	0.27
55	46.8749	3	2	3	1.93665	0.5

2. EXPERIMENTAL DETAILS

Di-peptides compounds Di-Leucine (LL) were used (Bachem, Switzerland: M-1535.0005 H-Leu-Leu-OH). PNTs were self-assembled by dissolving the dipeptide in the lyophilized form (Bachem, Switzerland) in 1,1,1,3,3,3-hexafluoro-2-propanol at a concentration of 20-100mg/ml. The stock solution was then diluted to a final concentration of 2mg/ml in doubledistilled water for the self-assembly process to occur. The diluted solution was deposited onto Pt-coated silicon substrates and left overnight for drying at room temperature.

The structural features were analyzed by X-ray diffraction (XRD) technique using a Rigaku X-ray diffractometer having a CuKα radiation source with λ = 1.541 Å.

Atomic Force Microscopy (AFM) measurements were carried out using a Veeco AFM Multimode Nanoscope (IV) MMAFM-2, Veeco microscopy. Local piezoelectric properties of the PNTs were visualized simultaneously by using Atomic Force Microscopy (AFM) in contact mode and piezoresponse force microscopy (PFM) methods [30]. The PFM technique is based on the converse piezoelectric effect, which is a linear coupling between the electrical and mechanical properties of a material. Since all ferroelectrics exhibit piezoelectricity, an electric field applied to a ferroelectric sample result in changes of its dimensions. To detect the polarization orientation the AFM tip is used as a top electrode, which is moved over the sample surface. Piezoresponse force microscopy relies on the linear strain response as a function of the external electric field. Regardless of this linear response that is inherent to materials without center of inversion symmetry, all materials dispose of a quadratic strain response in the electric field, known as electrostriction. Electrostriction therefore provides a local electromechanical response at the second harmonic of the AC voltage in piezoresponse force microscopy. This electrostrictive response provides valuable insight into the material properties in itself. It becomes particularly interesting in systems where the symmetry of the crystal does not allow for particular modes of deflection of the AFM, especially for lateral deflections. In this scenario, this type of microscopy provides a powerful imaging tool for local material defects like misfit dislocations. EFM (Electric Force Microscopy) oscillates a conducting AFM tip to sense electric force gradients. Usually, this is done in 2 passes - one to measure the topography in a standard dynamic mode and the second to "lift" a set amount above the recorded profile to measure electric field strength. Using the phase signal, a map of the gradient of the electric field is created. Kelvin Probe Force Microscopy (KFM) mode

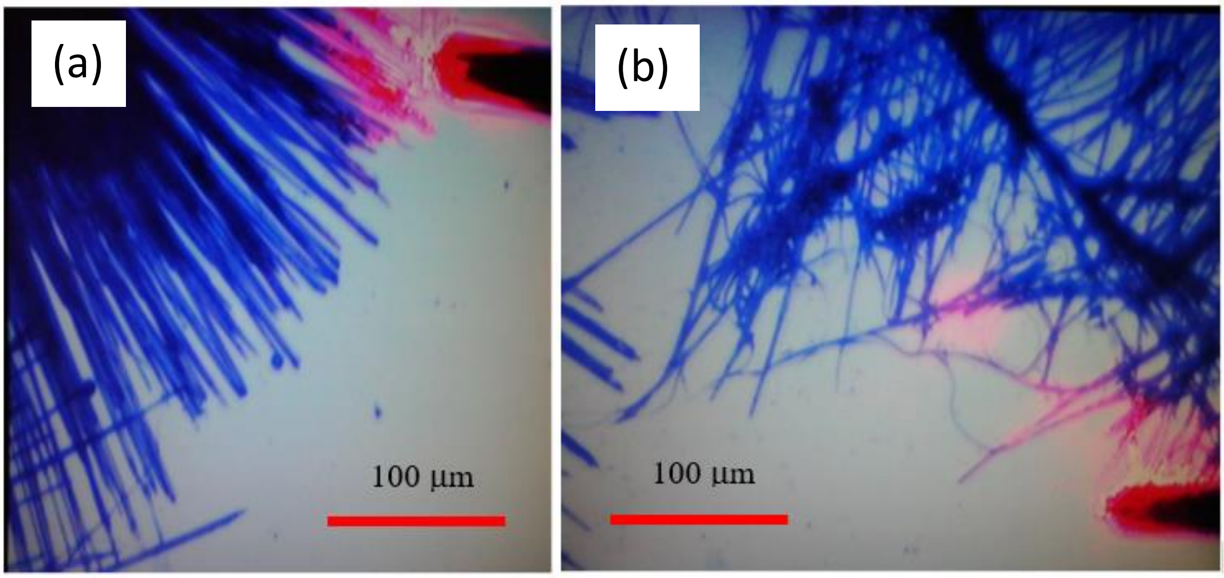

Figure 2. Optical images of LL PNTs.

measures the work function of the surface. It is also known as surface potential microscopy.

3. RESULTS AND DISCUSSION

Fig. 1 shows powder diffraction patterns of L,L-dileucine obtained in a similar way used for preparation of in this study for LL PNTs. Parameters of unit cell determined by XRD analysis (Table 1) is similar reported by C. Gorbitz [1]: a= 5.3524 Å, b= 16.7600 Å, c= 33.312 Å, V= 2988.3 $Å^3$. Rietveld-refined X-ray diffraction pattern of the dipeptide L,L-dileucine analysis was done using space group $P2_12_12_1$ (Table 1, Fig.1). Strong difference in unit cell volume (14%) and parameter a (12%) can be explain by presents of water in the structure.

Figures 2 show representative optical microscopy images of the investigated LL PNTs samples. As expected, as-grown PNTs demonstrate a variety of tubes of different lengths and diameters due to their spontaneous self-assembly on the substrate surface.

The cross section of the in-plane PFM (Figure 3c) shows the piezoelectric profile has a decrease in signal at the centre of the tube. It can be assumed that such a profile is typical for tubes with a large ratio of outer to inner diameter, where the internal cavity (in the centre of the section) has a significantly smaller effective thickness and the resulting signal is less than on the wall).

It is well known that the magnitude of the piezoresponce signal in PFM depends on measurement geometry and orientation. The figure 4 shows that with an arbitrary distribution of tubes on the surface of the substrate, the recorded signal changes both in magnitude and sign. In-plane (IP) PFM image of peptide nanotubes with rotation demonstrating apparent contrast reversal. Blue

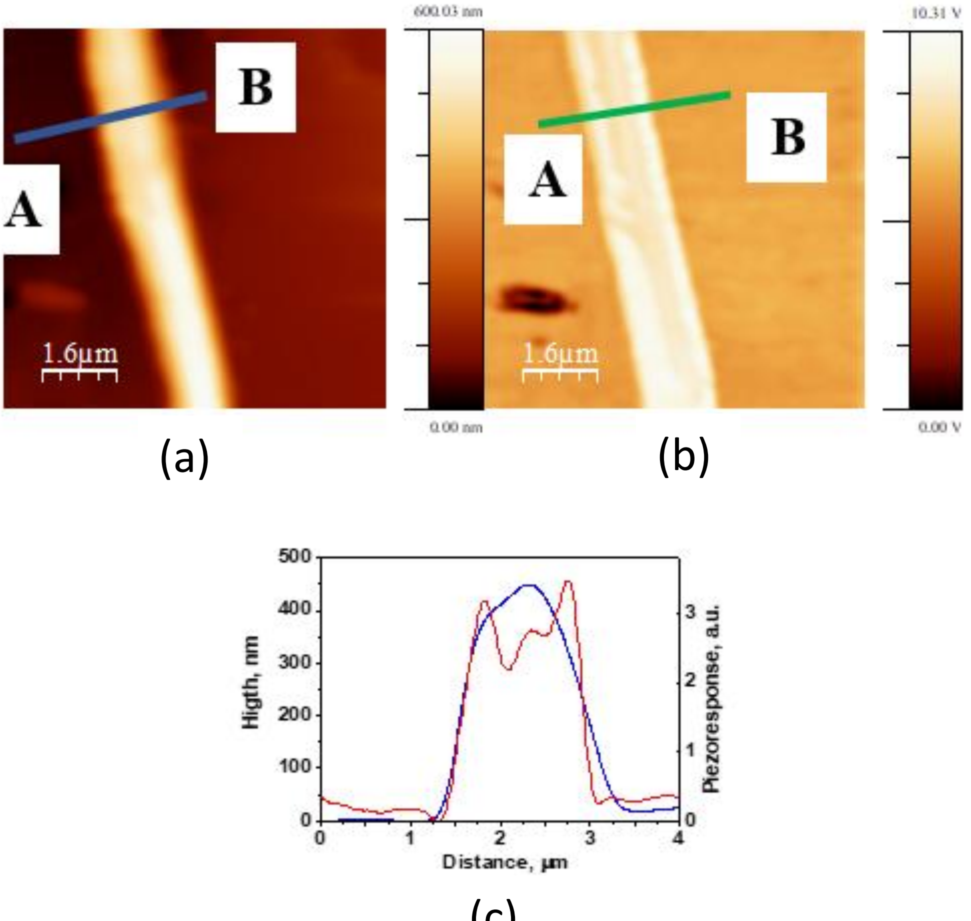

(a) (b)

(c)

Figure 3. LL PNTs. (a) Topography image. (b) In plane PFM image. Cross sections of AB - (c).

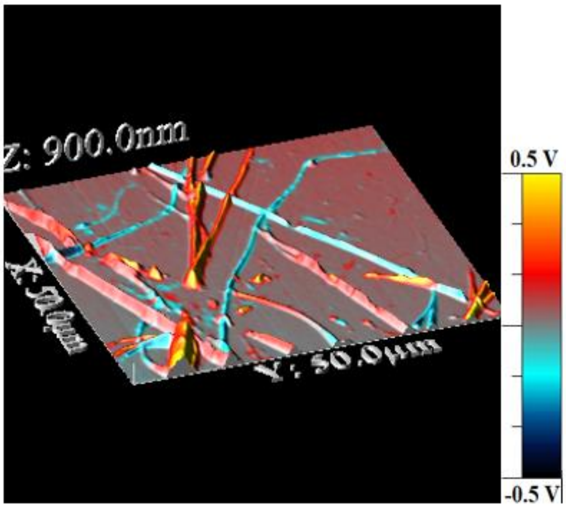

Figure 4. 3D LL PNTs topography and in-plane PFM (color) image.

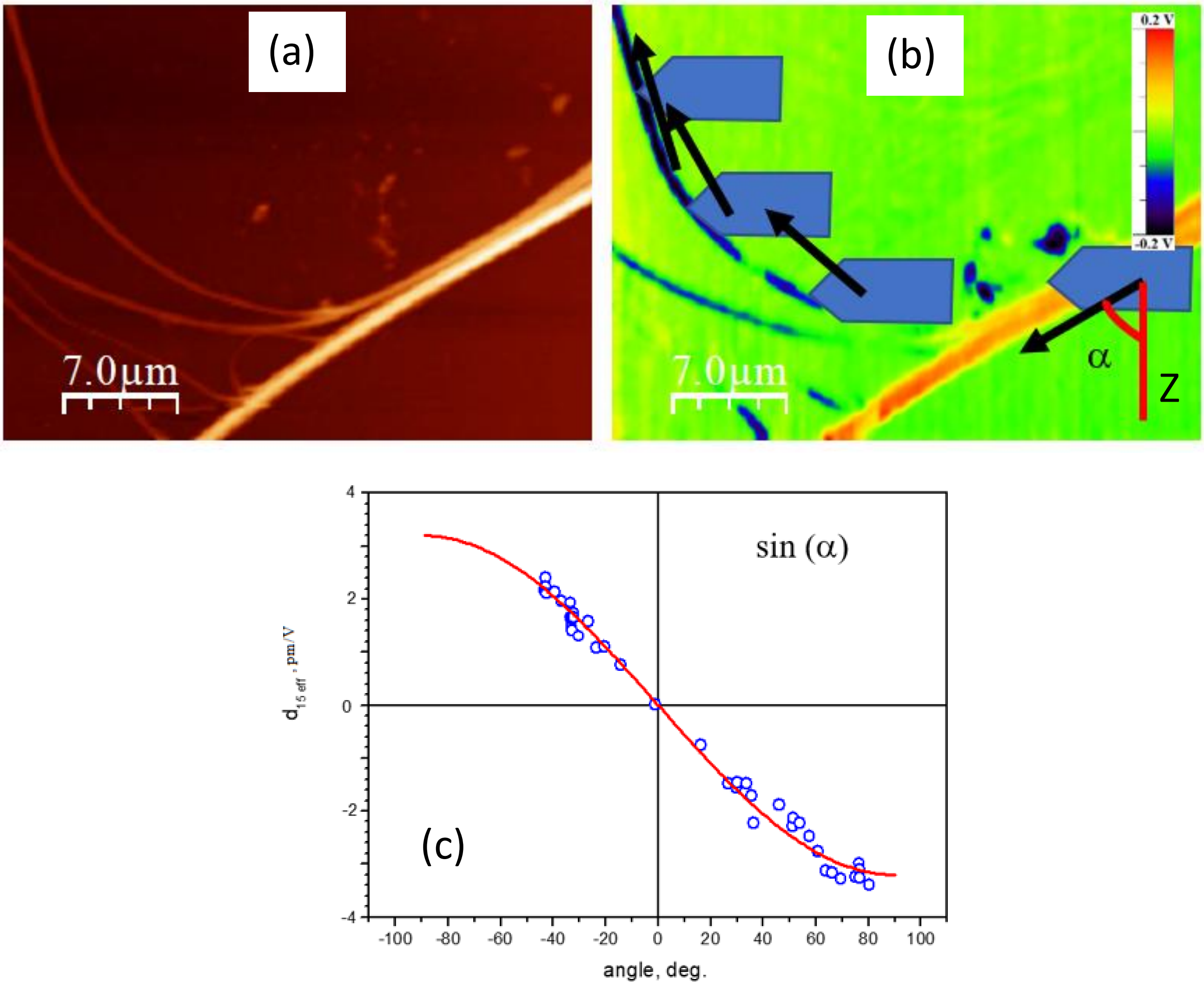

Figure 5. LL PNTs. (a) Topography and (b) PFM image. (c) IP signal angle dependences for representative tube.

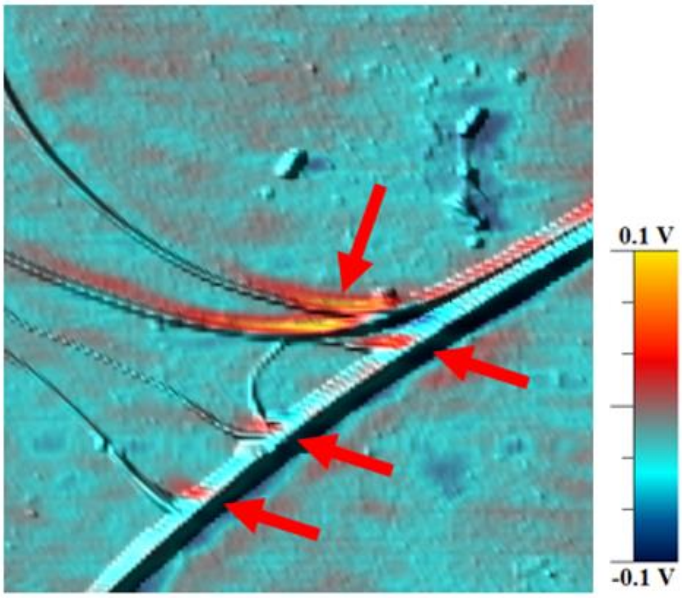

Figure 6. 3D LL PNTs. (a) Topography and KFM (color) image.

polarization orientations of the tubes.

For the arbitrary orientation of the crystal, possible to use equation, $d_{15}V_{ac}\sin\alpha$ (Fig. 5b), applies, where now angle is the angle between the scanning direction and the Z-axis. As shown in Figure 3d, we observed this dependence with the maximum value of 3.2 pm/V (Fig.5c).

Piezoelectric polarization leads to charge localization in the same way. For such a highly asymmetric case as tubes, when the polarization is directed along, one can expect an accumulation of charges at the ends of the tubes. In the case of a more significant reorientation of polarization, in the case of merging of two tubes, localization of charges can also be assumed. The method Kelvin Probe Force Microscopy (KFM) was used to study the charge distribution (Fig.6). It can be seen that at the points of contact of the nanotubes there is an increased contrast (indicated by arrows), which corresponds to the localization of the charges.

4. CONCLUSIONS

Experimental local measurements of the parameters of the piezo response of LL tubes and LL microcrystals were carried out. A study of the angular dependence of the orientation of the tubes showed agreement with the geometric measurement model. The effect of tube curvature on the electromechanical and electrostatic characteristics of the tubes was studied. The data obtained showed that LL-PNTs may be of the most promising interest for further use as stronger ferroelectric compounds.

ACKNOWLEDGMENTS

This work was developed in the scope of the Project “Agenda ILLIANCE” [C644919832-00000035 | Project no. 46], financed by PRR – Recovery and Resilience Plan under the Next Generation EU from the European Union. This work also was supported, in terms of TEMA Research Infrastructure equipment, by the projects UIDB/00481/2020 and UIDP/00481/2020 - Fundação para a Ciência e a Tecnologia; and CENTRO-01-0145-FEDER-022083 - Centro Portugal Regional Operational Programme (Centro2020), under the PORTUGAL 2020 Partnership Agreement, through the European Regional Development Fund.

REFERENCES

1. C. H. Gorbitz, Nanotube Formation by Hydrophobic Dipeptides, *Chem Eur J.*, **7**, 5153–5159 (2001).
2. E. Gazit, A possible role for π-stacking in the self-assembly of amyloid fibrils, *FASEB J.*, **16**, 77-83 (2002).
3. Silvia Marchesan, Attilio V. Vargiu and Katie E. Styan, The Phe-Phe Motif for Peptide Self-Assembly in Nanomedicine, *Molecules* **20**, 19775–19788 (2015).

4. Yingying Ding, Ding Li, Bin Li, Kai Zhao, Wei Du, Jinyun Zheng, Minghui Yang, A water-dispersible, ferrocene-tagged peptide nanowire for amplified electrochemical immunosensing, *Biosensors and Bioelectronics* **48** 281–286 (2013).
5. Ehud Gazit, Reductionist Approach in Peptide-Based Nanotechnology, *Annu. Rev. Biochem.* **87**, 533–53 (2018).
6. Sayanti Brahmachari, Zohar A. Arnon, Anat Frydman-Marom, Ehud Gazit, and Lihi Adler-Abramovich, Diphenylalanine as a Reductionist Model for the Mechanistic Characterization of β-Amyloid Modulators, *ACS Nano* **11**, 5960−5969 (2017).
7. R. C. Naber, K. Asadi, P. W. Blom, D. M. de Leeuw, and B. de Boer, Organic Nonvolatile Memory Devices on Ferroelectricity, *Adv. Mater.* **22**, 933 (2010).
8. S. H. Sung and B. W. Boudouris, Systematic Control of the Nanostructure of Semiconducting-Ferroelectric Polymer Composites in Thin Film Memory Devices, *ACS Macro Lett.* **4**, 293 (2015).
9. Zohar A. Arnon, Dorothea Pinotsi, Matthias Schmidt, Sharon Gilead, Tom Guterman, Aditya Sadhanala, Shahab Ahmad, Aviad Levin, Paul Walther, Clemens F. Kaminski, Marcus Fändrich, Gabriele S. Kaminski Schierle, Lihi Adler-Abramovich, Linda J. W. Shimon, and Ehud Gazit, Opal-like Multicolor Appearance of Self-Assembled Photonic Array, *ACS Appl. Mater. Interfaces* **10**, 20783−20789 (2018).
10. Wei-Hsien Hsieh, Jiahorng Liaw, Applications of cyclic peptide nanotubes (cPNTs), *Journal of food and drug analysis* **27**, 32-47 (2019).
11. Lihi Adler-Abramovich and Ehud Gazit, The physical properties of supramolecular peptide assemblies: from building block association to technological applications, *Chem. Soc. Rev.* **43**, 6881 (2014).
12. Michal Pellach, Sudipta Mondal, Linda J. W. Shimon, Lihi Adler-Abramovich, Ludmila Buzhansky, and Ehud Gazit, Molecular Engineering of Self-Assembling Diphenylalanine Analogues Results in the Formation of Distinctive Microstructures, *Chem. Mater.* **28**, 4341−4348 (2016).
13. Samaneh Beheshti, Sanela Martic, and Heinz-Bernhard Kraatz, Hierarchical Organization of Ferrocene–Peptides, *Chem. Eur. J.* **18**, 9099 – 9105 (2012).
14. Meital Reches and Ehud Gazit, Designed aromatic homo-dipeptides: formation of ordered nanostructures and potential nanotechnological applications, *Phys. Biol.* **3**, S10–S19 (2006).
15. Surajit Ghosh, Lihi Adler-Abramovich, Ehud Gazit, Sandeep Verma, Spacer driven morphological twist in Phe-Phe dipeptide conjugates, *Tetrahedron* **69**, 2004-2009 (2013).
16. Jianxiu Wang, Ding Li, Minghui Yang and Yi Zhang, A novel ferrocene-tagged peptide nanowire for enhanced electrochemical glucose biosensing, *Anal. Methods* **6**, 7161 (2014).
17. Magdalena Jaworska, Agata Jeziorna, Ewelina Drabik, and Marek J. Potrzebowski, Solid State NMR Study of Thermal Processes in Nanoassemblies Formed by Dipeptides, *J. Phys. Chem. C* 116, 12330−12338 (2012).
18. Gagandeep Kaur, Lihi A. Abramovich, Ehud Gazit and Sandeep Verma, Ultrastructure of metallopeptide-based soft spherical morphologies, *RSC Adv.* **4**, 64457–64465 (2014).
19. Sivan Yuran, Yair Razvag, Priyadip Das and Meital Reches, Self-assembly of azide containing dipeptides, *J. Pept. Sci.* **20**, 479–486 (2014).
20. Ran Wei, Cheng-Cheng Jin, Jing Quan, Hua-li Nie, Li-Min Zhu, A Novel Self-Assembling Peptide with UV-Responsive Properties, *Biopolymers* 101, 272-278 (2013).
21. Chilukuri Subbalakshmi, Sunkara V. Manoram and Ramakrishnan Nagaraj, Self-assembly of short peptides composed of only aliphatic amino acids and a combination of aromatic and aliphatic amino acids, *J. Pept. Sci.* **18**, 283–292 (2012).
22. T. Govindaraju, Spontaneous self-assembly of aromatic cyclic dipeptide into fibre bundles with high thermal stability and propensity for gelation, *Supramolecular Chemistry* **23**, 759–767 (2011).
23. Gokhan Demirel, Niranjan Malvadkar, and Melik C. Demirel, Control of Protein Adsorption onto Core-Shell Tubular and Vesicular, Structures of Diphenylalanine/Parylene, *Langmuir* **26(3)**, 1460–1463 (2010).
24. Gokhan Demirel, and Fatih Buyukserin, Surface-Induced Self-Assembly of Dipeptides onto Nanotextured Surfaces, *Langmuir* **27**, 12533–12538 (2011).
25. Balakrishnan Karthikeyan, Aswini Kumar Giri, Victor J. Hruby, Entrap and release of Phe–Phe nanotubes in sol–gel derived silicate matrix: study through nanosilver interaction, *J Sol-Gel Sci Technol* **72**, 534–542 (2014).
26. Andrei Kholkin, Nadav Amdursky, Igor Bdikin, Ehud Gazit, Gil Rosenman, Strong piezoelectricity in bioinspired peptide nanotubes, *ACS Nano* **4 (2)**, 610–614 (2010).
27. Igor Bdikin, Vladimir Bystrov, Svitlana Kopyl, Rui P. G. Lopes, Ivonne Delgadillo, Jose´ Gracio, Elena Mishina, Alexander Sigov, and Andrei L. Kholkin, Evidence of ferroelectricity and phase transition in pressed diphenylalanine peptide nanotubes, *Appl. Phys. Let.* **100**, 043702 (2012).
28. Igor Bdikin, Vladimir Bystrov, Ivonne Delgadillo, José Gracio, Svitlana Kopyl, Maciej Wojtas, Elena Mishina, Alexander Sigov, and Andrei L. Kholkin, Polarization switching and patterning in self-assembled peptide tubular structures, *J. Appl. Phys.* **111**, 074104 (7p) (2012).
29. S. Safaryan, V. Slabov, S. Kopyl, K. Romanyuk, I. Bdikin, S. Vasilev,P. Zelenovskiy, V. Shur, E. Uslamin, E. Pidko, A. Vinogradov,A. Kholkin, Diphenylalanine-Based Microribbons for Piezoelectric Applications via Inkjet Printing, *ACS Applied Materials & Interfaces* **10**, 12, 10543-10551 (2018).
30. A. Roelofs, T. Schneller, K Szot, and R Waser, Piezoresponse force microscopy of lead titanate nanograins possibly reaching the limit of ferroelectricity, *Applied Physics Letters* **81 (27)**, 5231-5233) (2002).

Nanomaterials Science & Engineering (NMS&E), Vol.5, No.1, 2023

Department of Mechanical Engineering
University of Aveiro
Aveiro 3810-193
Portugal

https://proa.ua.pt/index.php/nmse/

ISSN: 2184-7002

university of aveiro tema centre for mechanical technology and automation